scientific reports

OPEN

Advancing triple-negative breast cancer treatment through peptide decorated solid lipid nanoparticles for paclitaxel delivery

Tahereh Rahdari[1], Mohsen Mahdavimehr[2], Hossein Ghafouri[1]✉, Sorour Ramezanpour[3], Somayeh Ehtesham[4] & S. Mohsen Asghari[2]✉

Triple-negative breast cancer (TNBC) presents a global health challenge due to its aggressive behavior and limited treatment options. This study explores a novel therapeutic strategy using C-peptide-conjugated solid lipid nanoparticles (C-peptide-SLNs) for targeting paclitaxel (PTX) delivery in TNBC treatment. C-peptide, derived from endostatin, enhances efficacy by targeting overexpressed integrin αvβ3 receptors on TNBC cells. Characterization confirmed suitable particle size, stability, and encapsulation efficiency over 90%, with favorable release profiles for acidic tumor environments. In vitro, C-peptide-SLN-PTX markedly improved cytotoxicity against 4T1 carcinoma cells, with an IC_{50} of 1.2 μg/mL, compared to 3.4 μg/mL for SLN-PTX and 8.9 μg/mL for free PTX. Wound-healing assays verified significant inhibition of cell migration in 4T1 and MDA-MB-231 cell lines. Flow cytometry confirmed αv integrin targeting by C-peptide-SLN-PTX. In vivo studies in 4T1 tumor-bearing mice showed an 82% tumor volume reduction and prevented pulmonary metastasis, with normal liver enzyme levels indicating reduced toxicity. PET imaging revealed decreased tumor metabolic activity in treated groups, and immunohistochemical analyses demonstrated superior antitumor efficacy with reduced Ki-67 expression and apoptosis induction (p53 upregulation, Bcl-2 downregulation). These findings highlight the potential of C-peptide-SLNs as an effective targeted PTX delivery system for TNBC, offering promising avenues for enhancing cancer treatment strategies.

Keywords SLNs, C-peptide, Paclitaxel, Targeted delivery, Triple-negative breast cancer, Therapeutic efficacy

Cancer remains a formidable global health challenge, characterized by its uncontrolled cell proliferation and invasive capabilities, significantly contributing to mortality rates worldwide. Among the myriad of cancer types, breast cancer emerges as the most prevalent malignancy affecting women, accounting for approximately 30% of all female cancers[1]. Within this spectrum, particularly TNBC is particularly aggressive, defined by the absence of estrogen receptors, progesterone receptors, and HER2 expression. This lack of receptor expression renders TNBC resistant to many existing targeted therapies, resulting in poor clinical outcomes and limited treatment options for affected individuals[2–5]. PTX, a chemotherapeutic agent from the taxane family, is widely used in treating various cancers, including breast cancer. Its mechanism involves stabilizing microtubules by enhancing tubulin polymerization and inhibiting depolymerization, leading to mitotic spindle disruption, cell cycle arrest at the G2/M phase, and apoptosis in cancer cells[6]. Despite its efficacy, PTX is associated with significant side effects such as myelosuppression, neurotoxicity, and cardiotoxicity, which can necessitate treatment discontinuation. Additionally, PTX's poor solubility limits its bioavailability, underscoring the need for advanced drug delivery systems to enhance its therapeutic potential[7–12].

Nanoparticles have emerged as a versatile platform for improving the therapeutic efficacy of chemotherapeutic drugs, significantly enhancing drug administration and effectiveness in cancer therapy[13–15]. Solid lipid nanoparticles (SLNs) have shown considerable promise as nanocarriers for delivery of chemotherapeutic agents[16,17]. Encapsulating PTX within SLNs offers several advantages, including improved bioavailability of hydrophobic drugs like PTX by enhancing solubility and stability, ensuring higher concentrations reach the

[1]Department of Biology, Faculty of Sciences, University of Guilan, Rasht, Iran. [2]Institute of Biochemistry and Biophysics, University of Tehran, Tehran, Iran. [3]Department of Chemistry, K. N. Toosi University of Technology, Tehran, Iran. [4]Department of Biology, Parand Branch, Islamic Azad University, Parand, Iran. ✉email: h.ghafoori@guilan.ac.ir; sm.asghari@ut.ac.ir

tumor site. SLNs also mitigate systemic toxicity by facilitating drug delivery to tumors, sparing normal tissues and alleviating common side effects. The controlled release mechanism of SLNs can be tailored to specific pharmacokinetic profiles[18–20].

The therapeutic potential of SLNs can be further enhanced through the conjugation of tumor targeting ligands[19,21–23]. Integrins, which play a pivotal role in cancer progression by mediating essential signaling pathways influencing tumor cell adhesion, migration, and invasion, are prime targets. Targeting these integrins with ligands, such as peptides, facilitates selective delivery of therapeutics to tumor sites while minimizing off-target effects. Disrupting integrin-mediated pathways can inhibit critical processes like cell adhesion, migration, and invasion[24,25].

Our research focuses on developing a novel peptide derived from human endostatin, named C-peptide, that serves as a functional analog of endostatin, aimed at enhancing antitumor effects while improving stability and therapeutic efficacy. We indicated that the C-terminal segment of endostatin, particularly residues 123 to 184, is crucial for inhibiting cell proliferation, migration, and tumor growth[24]. To optimize the peptide's therapeutic potential, we systematically eliminated non-essential segments, including the β-hairpin region (residues 145–163), a short β-strand (residues 172–175), and residues 175 to 184, which previous studies indicated were not vital for endostatin's biological activity. The synthesized C-peptide features a sequence of 30 amino acids: $_2$HN-SDPNGRRLTESYCETWRTEAPSSCHHAYIV-COOH.

Typically, peptides exhibit a short serum half-life due to rapid renal filtration and enzymatic degradation; however, conjugating the C-peptide to SLNs significantly enhances its stability and therapeutic effectiveness. By integrating this novel C-peptide with SLNs, we aim to achieve targeted delivery of PTX directly to tumor sites. This design is intended to improve drug accumulation at the tumor site while minimizing the systemic toxicity frequently associated with conventional chemotherapy. The targeted binding capability of the C-peptide to integrin receptors, often overexpressed on TNBC cells, further strengthens the therapeutic potential of this approach.

Results and discussion

Characterization of nanoparticles

Physicochemical characterization of nanoparticles

The physicochemical properties of SLNs were evaluated using DLS to determine their size, surface charge, and homogeneity. The initial particle size of SLNs was measured using DLS, showing a mean size of 240 nm with a PDI of 0.3. Upon C-peptide conjugation, the size of SLN changed to 291 nm with a PDI of 0.2. The size of SLN-PTX increased to 315 nm with a PDI of 0.08, likely due to effective drug encapsulation. The size of C-peptide conjugated-SLN-PTX further rose to 362 nm with a PDI of 0.08 (Fig. S3), suggesting successful surface functionalization and a controlled increase in size due to the added molecular layer from the conjugated peptide.

The zeta potential values for both blank-SLN and SLN-PTX were – 23 mV, indicating no significant difference between them. This suggests that the incorporation of PTX into SLN did not affect its colloidal stability. However, upon conjugation with the peptide, the surface charge decreased to -10 mV, confirming the formation of an amide bond between the carboxylate groups on the SLN surface and the peptide's amino terminus. This reduction in surface charge is due to the shielding of some carboxyl groups (Fig. 1A–C).

Previous studies have shown that negatively charged nanoparticles can reduce clearance and improve blood compatibility, thereby enhancing the efficiency of anti-cancer drug delivery to tumor sites through electrostatic repulsion with cellular surfaces[26]. The uniform size distribution, negative surface charge, and successful incorporation of therapeutic agents (PTX and peptides) suggest that these nanoparticles are well-suited for biomedical applications. After a 4-month storage period at -20 °C, the mean hydrodynamic diameter (HD), PDI, and zeta potential of the SLNs were re-evaluated using DLS. The measurements indicated that the size and zeta potential of the nanoparticles remained largely unchanged from the initial values, demonstrating that the SLNs maintained their stability throughout the storage period (data not shown).

The morphology of the nanoparticles was examined using SEM and AFM. The micrographs revealed spherical nanoparticles with a uniform size, making them suitable for drug delivery. Morphological analysis showed that the conjugation of the peptide and entrapment of PTX did not alter the SLNs' shape. The nanoparticle sizes were consistent with the DLS measurements (Fig. 1D).

Spectroscopic analyses

FTIR spectroscopy was used to confirm the formation of nanoparticles and the interactions of functional groups (Fig. 1H). The FTIR data spanned from 475 to 4000 cm^{-1}. In blank SLN, key peaks included 2920 and 2854 cm^{-1} (C–H stretch in $–CH_2$ groups), 1710 cm^{-1} (C = O stretching), 1110 cm^{-1} (C–O–C stretching), and 3400 cm^{-1} (O–H stretching)[27,28]. PTX exhibited peaks at 3470 cm^{-1} (O-H and N-H stretching) and 1708 cm^{-1} (C = O stretching). These peaks disappeared in the SLN-PTX formulation, indicating complete entrapment within the lipid matrix[18,29–31]. Two main characteristic peaks were observed for the peptide: the stretching vibrations of the amidic C = O band at 1645 cm^{-1}, which overlapped with the vibrations of the carbonyl group of COOH, and the peak at 1511 cm^{-1}, which corresponds to N-H bending[32]. For C-peptide-SLN conjugates, characteristic peaks were observed at 1645 cm^{-1} (amidic C = O stretching) and 1511 cm^{-1} (N-H bending), confirming peptide conjugation. The decrease in the 1785 cm^{-1} band further supported the formation of amide bonds between the peptide's NH_2 group and the SLNs' COOH group (Fig. 1E).

The crystal structure of the nanoparticles was analyzed by XRD. In PTX-loaded SLNs, the diffraction peaks of PTX disappeared, showing that PTX was effectively encapsulated into SLN (Fig. 1F).

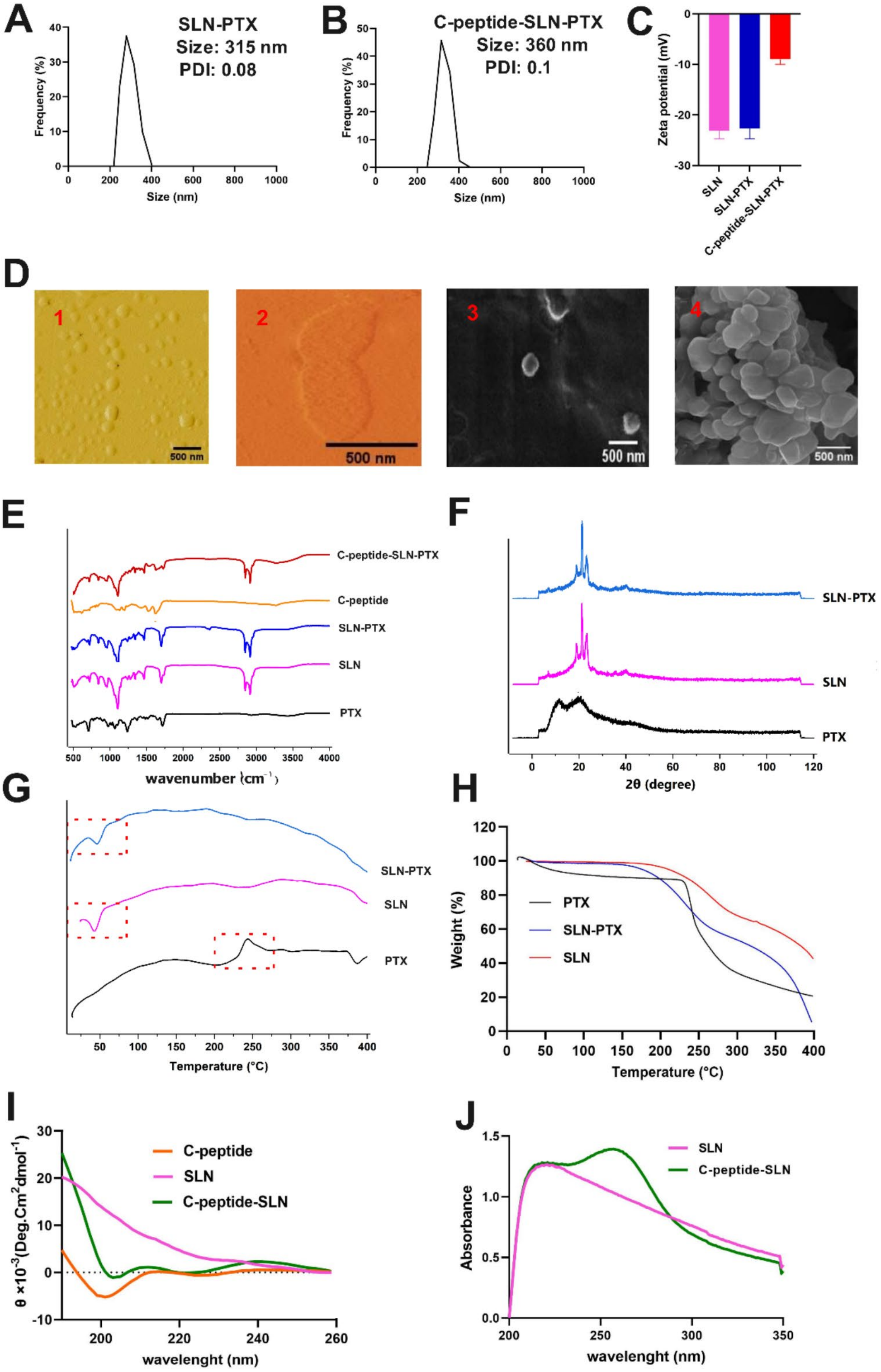

Fig. 1. Characterization of nanoparticles. (**A**) Size and PDI of SLN-PTX analyzed by DLS. (**B**) Size and PDI of C-peptide-SLN-PTX analyzed by DLS. (**C**) Zeta potential of nanoparticles. (**D**) Morphological analysis of nanoparticles by AFM and FE-SEM, scale bar: 500 nm (AFM images: (1) SLN-PTX, (2) C-peptide-SLN-PTX. FE-SEM images: (3) SLN-PTX, (4) C-peptide-SLN-PTX). (**E**) FTIR analysis of nanoparticles (500–4000 cm^{-1}). (**F**) XRD analysis. (**G**) DSC measurement. (**H**) TGA analysis. (**I**) secondary structure analysis of C-peptide before and after conjugation using CD. (**J**) UV-visible analysis.

Thermal analysis

Differential Scanning Calorimetry (DSC) was used to measure heat flow associated with thermal transitions. The endothermic melting peaks of stearic acid and precirol at 53 °C indicated that the lipid core in Blank-SLN and SLN-PTX was in a solid state (Fig. 1G). Free PTX showed a sharp endothermic peak at 205 °C, just before an exothermic degradation peak, revealing its crystalline form. The absence of the PTX endothermic peak in SLN-PTX formulations indicates that PTX has been converted from a crystalline to a dispersed amorphous state within the nanoparticles. This also suggests a strong PTX-lipid interaction, contributing to the slower release of PTX from SLN-PTX. These findings align with previous studies (Fig. 1G)[11,18,33–36].

TGA was undertaken to examine the thermal stability and purity of blank SLNs and PTX-loaded SLNs. The TGA results showed that SLN-PTX followed the weight-loss pattern of blank SLNs, indicating successful PTX loading. While free PTX showed rapid weight loss, both blank and PTX-loaded SLNs exhibited gradual weight loss, suggesting higher thermal stability for SLN-PTX compared to free PTX, consistent with other research findings (Fig. 1H)[37–39]. The DSC and TGA results indicate that the SLNs provide a stable environment for encapsulated drugs.

Spectroscopic confirmation of peptide conjugation

The secondary structure of C-peptide, both before and after its conjugation to SLN, was analyzed using CD spectroscopy (Fig. 1I). The C-peptide exhibited a random coil structure with negative molecular ellipticity at 195–200 nm. Upon conjugation to SLNs, the peptide's overall unordered structure is predominantly retained. The slight structural modifications observed likely result from interactions with the nanoparticle surface but do not compromise the peptide's overall conformational characteristics.

Peptide conjugation to SLNs was confirmed using UV-Vis spectra. The synthesized SLN exhibited a prominent absorbance peak around λmax ~ 225 nm, attributed to solid lipids used in the preparation (stearic acid and precirol). However, the Peptide conjugated-SLN showed a new absorption band at λmax ~ 280 nm, indicative of tryptophan and tyrosine residues in the C-peptide structure, confirming the binding of the C-peptide to SLNs (Fig. 1J).

The UV–Vis absorption spectra and the calibration curve of PTX are presented in Figure S4. The entrapment efficiency of PTX was calculated to be 90 ± 2.4%. The encapsulation of Fe_3O_4 into SLN-PTX is confirmed by XRD (Figure S5). The specific binding of C-peptide-SLN-PTX to αvβ integrin receptors is confirmed by MR imaging. As shown in Figure S6, a higher dose of anti-αvβ can restrict the binding of C-peptide-SLN-PTX, as indicated by a decrease in T_2-MR intensity signals. Figure 2 illustrates the designed C-peptide-SLN-PTX nanoparticle.

Drug release profile

The release profile of PTX from Free PTX, SLN-PTX, and C-peptide-SLN-PTX was studied at pH 4.7, 5.5, 6, and 6.5 simulating the acidic conditions within the tumor cell microenvironment and the subcellular organelles,

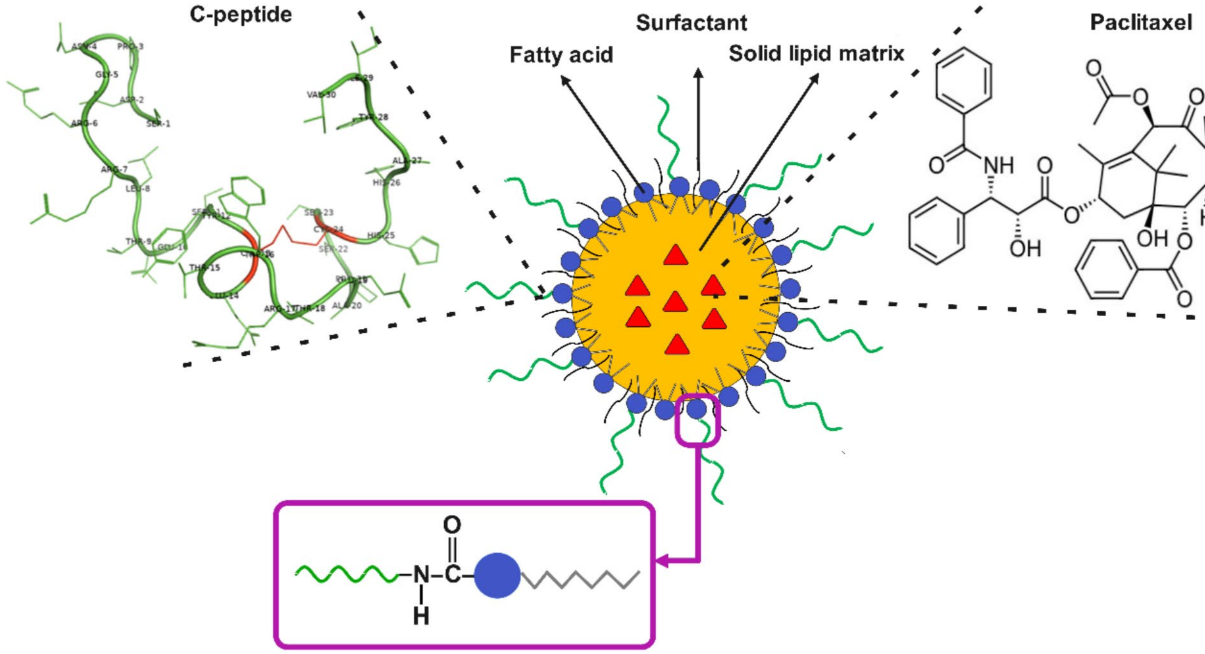

Fig. 2. Schematic of peptide-decorated SLN-PTX nanoparticle. SLNs were prepared via hot homogenization technique combined with subsequent ultra-sonication. During the synthesis process, PTX was incorporated into the molten lipid phase. This was followed by adding an aqueous phase containing Poloxamer 407 and soybean lecithin while undergoing homogenization. C-peptide, derived from endostatin with the sequence $_2$HN-SDPNGRRLTESYCETWRTEAPSSCHHAYIV-COOH, was covalently conjugated to the carboxylic groups on the SLN surface through its N-terminal using EDC & NHS.

and at pH 7.4, representing the physiological pH of blood (Fig. 3A). Additionally, pH 8.5 was used to further validate pH-dependent behavior[40,41]. Results showed that PTX-loaded SLN exhibited sustained release due to the homogeneous dispersion of encapsulated PTX throughout the solid lipid matrix and its strong interaction with the lipid matrix. Sustained release enables PTX to maintain an effective concentration in the bloodstream for an extended period. The presence of the peptide did not disrupt the release of PTX from SLN. As shown in the results, SLNs exhibited pH-dependent PTX release behaviors, but the release of free PTX was pH-independent. Under acidic conditions, the release of PTX from SLNs was faster and facilitated, whereas at pH 7.4 and pH 8.5, it required a significantly longer duration. The pH-dependent release is attributed to the protonation of the carboxyl group of stearic acids and precirols (pKa ~ 5), which reduces electrostatic attractions and leads to the loosening of the structure. As the shell of the nanoparticle becomes loose, the release of PTX becomes easier[42]. The release characteristic of PTX-loaded SLN ensures the release of PTX in tumor cells. After the circulation of PTX-loaded SLN in the blood system and reaching the tumor site, where the environment is acidic, the nanocarrier will become looser and release PTX in a controlled manner. Then the nanocarrier gradually degrades[30]. The targeting of αvβ3 receptors, combined with sustained and pH-dependent release from C-peptide-conjugated SLN-PTX, represents a major advancement in cancer therapy. This innovative strategy enhances the specificity of PTX delivery to tumor cells and ensures controlled release in the acidic tumor microenvironment. By utilizing integrin targeting, this approach maximizes therapeutic efficacy while minimizing systemic side effects, paving the way for more effective cancer treatments.

For any new nanoparticle designed for in vivo studies, it is essential to assess colloidal stability before conducting in vivo experiments. This is because if nanoparticles aggregate in serum homogenate, for example, they could also aggregate upon injection into the blood (as serum is a blood component). This could lead to clot formation and affect the drug delivery properties of nanoparticles due to differences in drug release from single nanoparticles compared to nanoparticle clusters[43]. To assess cluster formation, possibly causing a rise in particle size distribution (PSD), SLNs were exposed to serum and analyzed for changes over a period of time. According to Fig. 3B, the results showed that the size distribution did not vary, indicating that the SLNs were stable.

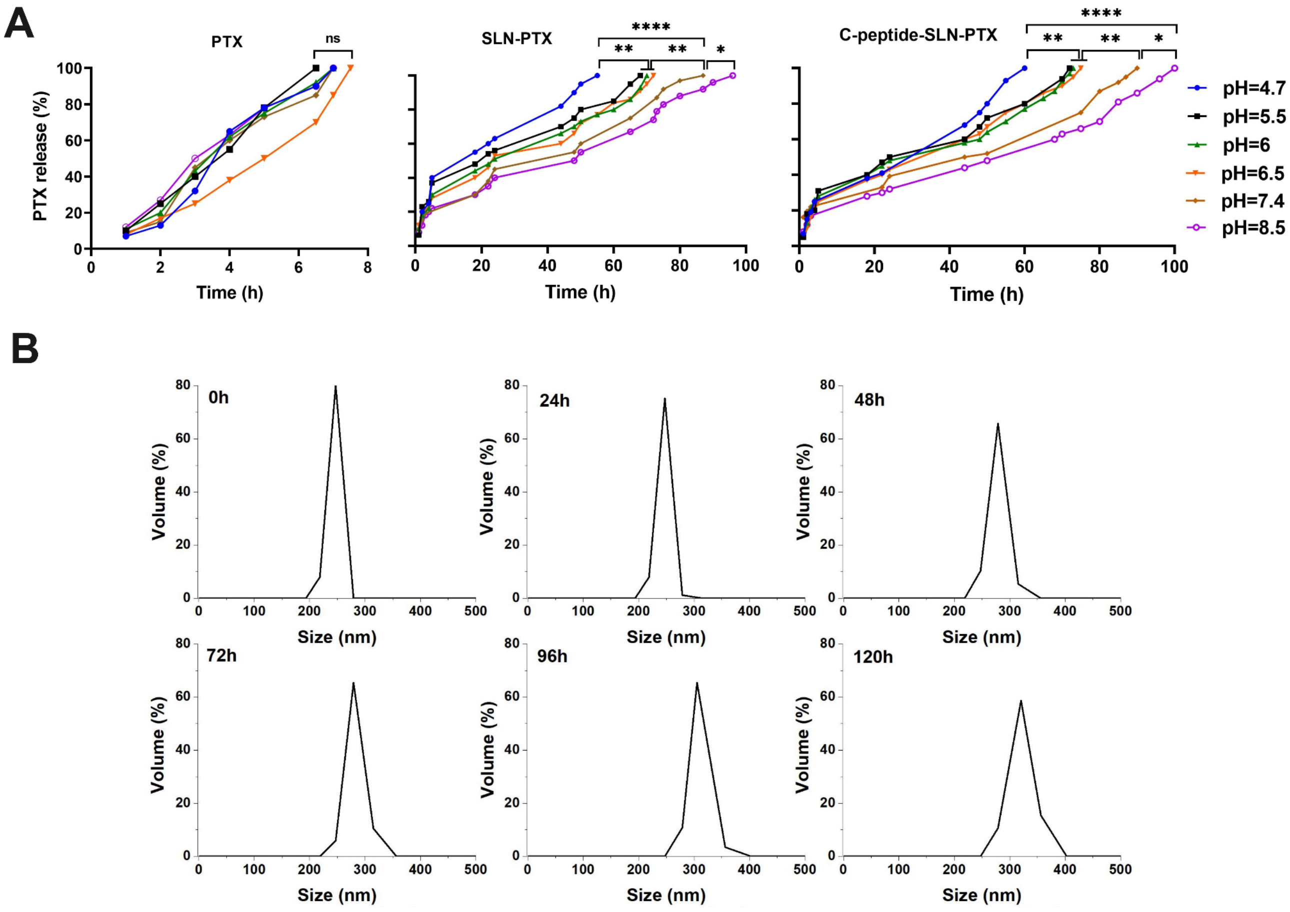

Fig. 3. Release and serum stability studies. (**A**) Drug release profiles of free PTX, SLN-PTX and C-peptide-SLN -PTX in PBS at pH 4.7, 5.5, 6, 6.5, 7.4 and 8.5. The significant differences among different pHs were analyzed using Prism 8 software (two-way ANOVA: $n = 3$, $^{****}P < 0.0001$, $^{***}P < 0.001$, $^{**}P < 0.01$, $^{*}P < 0.05$, or ns: not significant). (**B**) Serum stability study of SLNs analyzed by DLS, showing the stability of the nanoparticles under serum conditions over time.

In vitro cytotoxicity

To assess the cytotoxic effects of various formulations, including SLN, free PTX, C-Peptide, SLN-PTX, and C-peptide-SLN-PTX, MTT assays were conducted on triple-negative breast cancer cells, 4T1 mammary carcinoma tumor (MCT) and MDA-MB-231 cells, at different concentrations equivalent to PTX over 24 h. The results of cytotoxicity on 4T1 cells showed that SLNs alone did not affect cell viability, which was comparable to the control (non-treated cells), indicating their biocompatibility and potential for effective drug delivery. The IC_{50} value for free PTX was determined to be 8.9 µg/ml, whereas SLN-PTX exhibited a lower IC_{50} of 3.4 µg/ml. This suggests that encapsulating PTX in SLNs enhances its efficacy through improved solubility and sustained release. The free C-peptide had an IC_{50} value of 10.7 µg/ml, while C-peptide-SLN-PTX showed a significantly lower IC_{50} of 1.2 µg/ml, demonstrating the peptide's role in targeting and enhancing antitumor activity when conjugated to the nanoparticles. These data are illustrated in Fig. 4A. The results of the MTT assay on MDA-MB-231 cells revealed similar findings. The IC_{50} values for free PTX, C-peptide, SLN-PTX, and C-peptide-SLN-PTX were 9.8 µg/ml, 8.3 µg/ml, 4 µg/ml, and 1 µg/ml, respectively (Fig. 5A).

This finding aligns with other studies that indicate nanoparticle formulations can significantly enhance drug uptake and retention in cancer cells while reducing off-target effects compared to conventional free drug therapies[18].

Cell migration

Cell migration is a critical process for angiogenesis and tumor invasion. To evaluate the antimigrative effects of the nanoparticles, a wound-healing assay was performed on 4T1 and MDA-MB-231 cells, using nanoparticles at 70% of their IC_{50} concentrations. The cells were incubated for 24 and 48 h. The extent of cell migration into the wound area was assessed and compared across various groups: no treatment, SLN, PTX, C-peptide, SLN-PTX, and C-peptide-SLN-PTX. The results indicated that cells migrated to fill the wound area in the no-treatment and SLN groups within 48 h. In contrast, migration was significantly inhibited by PTX, C-peptide, SLN-PTX, and C-peptide-SLN-PTX. Among these, C-peptide-SLN-PTX demonstrated the greatest inhibition of cell migration, showing a significantly higher suppression rate compared to the other treatments ($P < 0.0001$) (Figs. 4B and C and 5B and C and see the original images of the scratch assay on 4T1 cells in Figure S7). This enhanced inhibition is likely due to the combined effects of targeted delivery and controlled drug release. The endostatin-derived peptide targets integrin $\alpha v\beta_3$, which is crucial for cell adhesion and migration, thereby disrupting these processes. Additionally, the SLN formulation improves PTX solubility and stability. These findings suggest that C-peptide-SLN-PTX holds promise for further investigation into its role in cancer therapy and metastasis management, pending in vivo validation.

Specific binding of peptide-conjugated nanoparticles' to the αv integrin receptors

As mentioned earlier, C-peptide is derived from human endostatin, which interacts with $\alpha v\beta_3$ integrins, prominent ligands on tumor cell surfaces. Accordingly, we elucidated the binding specificity of C-peptide to αvβ3 integrins via a competitive binding assay utilizing an anti-αv antibody. 4T1 cells underwent treatment with control (no treatment), C-peptide at 70% IC_{50}, SLN-PTX at 70% IC_{50}, and C-peptide-SLN-PTX at 30% and 70% IC_{50} concentrations. The anti-αv integrin antibody was included in each mixture. After a 3-hour incubation, a FITC-labeled secondary antibody was applied for an additional hour to bind the primary antibodies. Upon washing, which removed unbound probes, fluorescence intensity was analyzed via flow cytometry. In the absence of the peptide (control and SLN-PTX groups), the primary antibody exhibited maximal binding to αv integrin receptors, resulting in the highest fluorescent signal. Increasing concentrations of C-peptide-SLN-PTX led to a dose-dependent reduction in fluorescence intensity, confirming the peptide's specificity for αv integrin receptors. At 70% IC_{50}, both free C-peptide and C-peptide-SLN-PTX occupied nearly all available binding sites for the primary antibody, resulting in negligible fluorescent signals ($P < 0.01$). Quantitative analysis revealed that the binding of C-peptide-SLN-PTX to αv integrin receptors was approximately 15% at 0.36 µg/ml and 45% at 0.84 µg/ml. In comparison, the binding percentage for free C-peptide (at 7.4 µg/ml) was 48%. The control group exhibited primary antibody binding of 50%, while no binding was detected for SLN-PTX (Fig. 6). Statistical analysis demonstrated significant differences in binding of C-peptide-SLN-PTX compared to SLN-PTX ($P < 0.01$) and C-peptide ($P < 0.05$).

To further investigate the binding capacity of the drug delivery system, in vitro magnetic resonance (MR) imaging studies were conducted on 4T1 cells overexpressing integrin $\alpha v\beta_3$. Oleic acid-coated Fe_3O_4 was encapsulated within the nanoparticles to serve as an MR contrast agent. Cells were incubated with the nanoparticles (70% of IC_{50} concentration) and anti-integrin αv antibody (at concentrations of 100, 200, and 300 ng/ml) for four hours. Post-incubation, cells were washed to remove unbound nanoparticles, and MR imaging was performed for visual analysis. The MR imaging results demonstrated that cells treated with C-peptide-SLN-PTX-Fe_3O_4 exhibited significantly enhanced signal contrast compared to those treated with non-targeted SLN-PTX-Fe_3O_4, confirming specific binding to αv integrin receptors ($P < 0.01$). Additionally, higher concentrations of the anti-integrin αv antibody significantly reduced the binding of C-peptide-SLN-PTX-Fe_3O_4, as evidenced by a marked decrease in MR signal intensity (Figure S6).

Tumor growth inhibition

To evaluate the in vivo effectiveness of C-peptide-decorated solid lipid nanoparticles (SLNs), 4T1 mammary carcinoma tumor (MCT) cells were implanted into Balb/c mice. Eleven days post-implantation, when tumors reached approximately 100 mm^3, the mice were divided into four treatment groups: PBS (control), PTX (paclitaxel), SLN-PTX, and C-peptide-SLN-PTX, with six mice per group. Treatments were administered intravenously every four days over a 36-day period (Fig. 7A). Throughout the study, tumor volume, body weight,

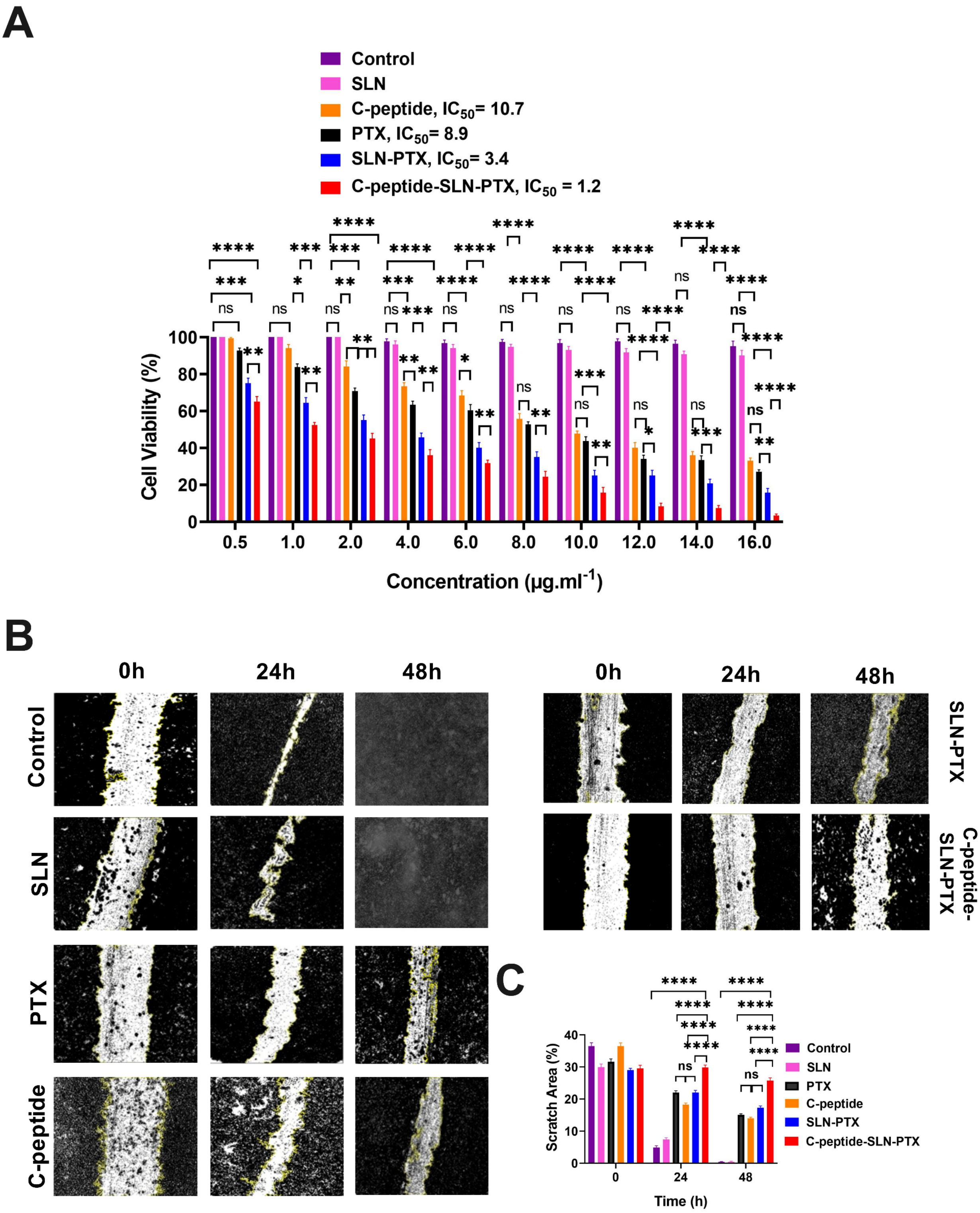

Fig. 4. Cell viability and migration assays studies on 4T1 MCT cells. (**A**) Viability of 4T1 MCT cells treated with various formulations, including SLN, C-peptide, PTX, SLN-PTX, C-peptide-SLN-PTX at concentrations equivalent to PTX (0.5, 1, 2, 4, 6, 8, 10, 12, 14, 16 μg/ml) after 24 h. Cell viability was measured through the MTT assay, and data were analyzed with Prism 8 software (two-way ANOVA, $n = 3$, mean ± SEM, $^{****}P < 0.0001$, $^{***}P < 0.001$, $^{**}P < 0.01$, $^{*}P < 0.05$, or ns: not significant). (**B**) Scratch migration assay of 4T1 MCT cells treated with PBS (control), SLN, PTX, C-peptide, SLN-PTX, and C-peptide-SLN -PTX. Cells were incubated for 0, 24, and 48 h. (**C**) Wound areas were quantified using ImageJ and Prism 8 software (two-way ANOVA, $n = 3$, mean ± SEM, $^{****}P < 0.0001$, $^{***}P < 0.001$, $^{**}P < 0.01$, $^{*}P < 0.05$, or ns: not significant).

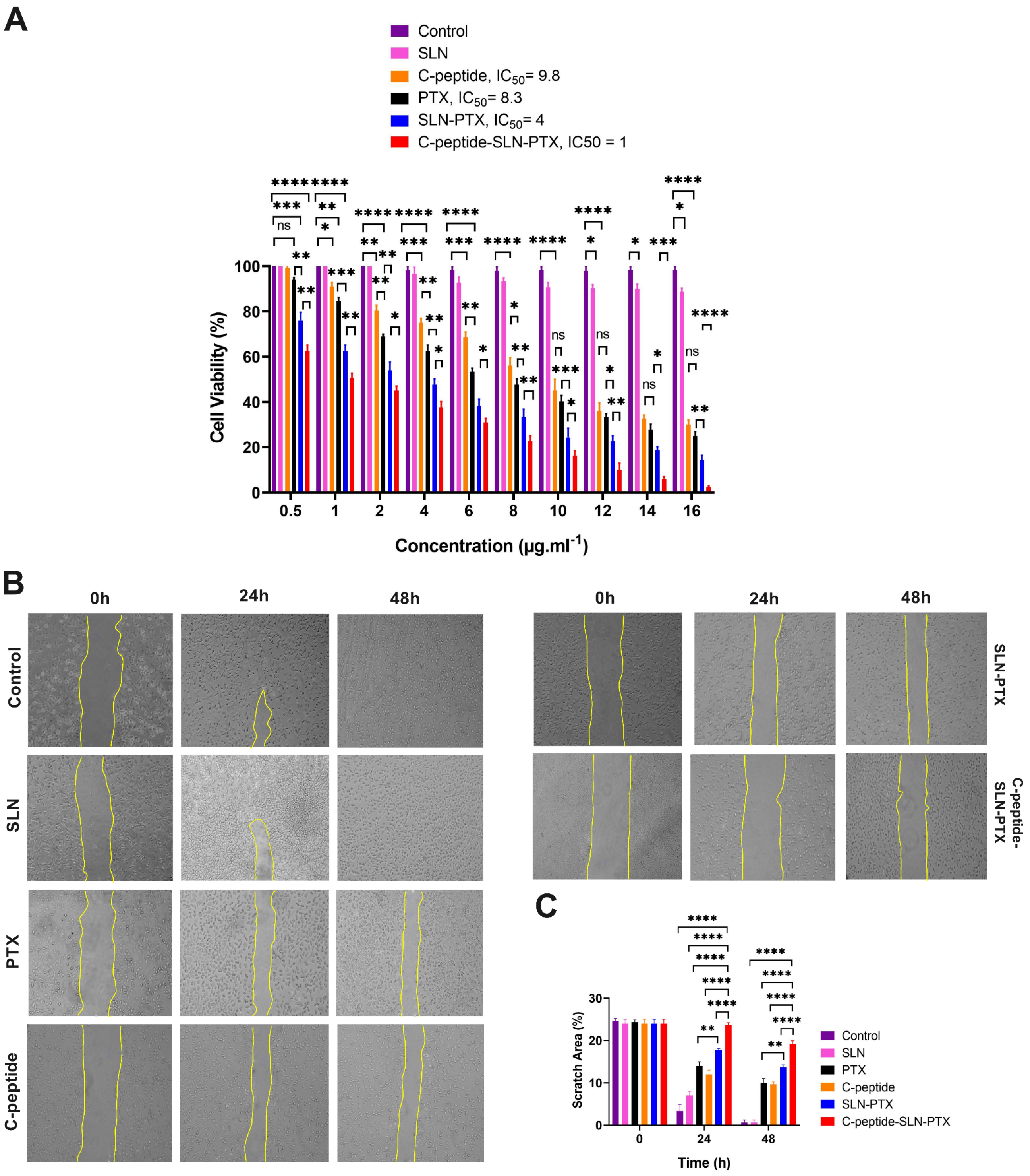

Fig. 5. Cell viability and migration assays studies on MDA-MB-231 cells. (**A**) Viability of MDA-MB-231 cells treated with SLN, C-peptide, PTX, SLN-PTX and C-peptide-SLN-PTX at concentrations equivalent to PTX (0.5, 1, 2, 4, 6, 8, 10, 12, 14, 16 µg/ml) after 24 h. The MTT assay was utilized to assess cell viability. The data were analyzed using Prism 8 software, applying a two-way ANOVA. The results are presented as mean ± SEM, with significance levels indicated as follows: ****$P < 0.0001$, ***$P < 0.001$, **$P < 0.01$, *$P < 0.05$, and ns for not significant ($n = 3$). (**B**) The scratch migration assay was conducted on MDA-MB-231 cells treated with various conditions: PBS (control), SLN, PTX, C-peptide, SLN-PTX, and C-peptide-SLN-PTX. Cells were incubated for durations of 0, 24, and 48 h. **C**: Wound areas were quantified using ImageJ and Prism 8 software. The analysis employed a two-way ANOVA, with results expressed as mean ± SEM. Significance levels were determined as follows: ****$P < 0.0001$, ***$P < 0.001$, **$P < 0.01$, *$P < 0.05$, and ns for not significant ($n = 3$).

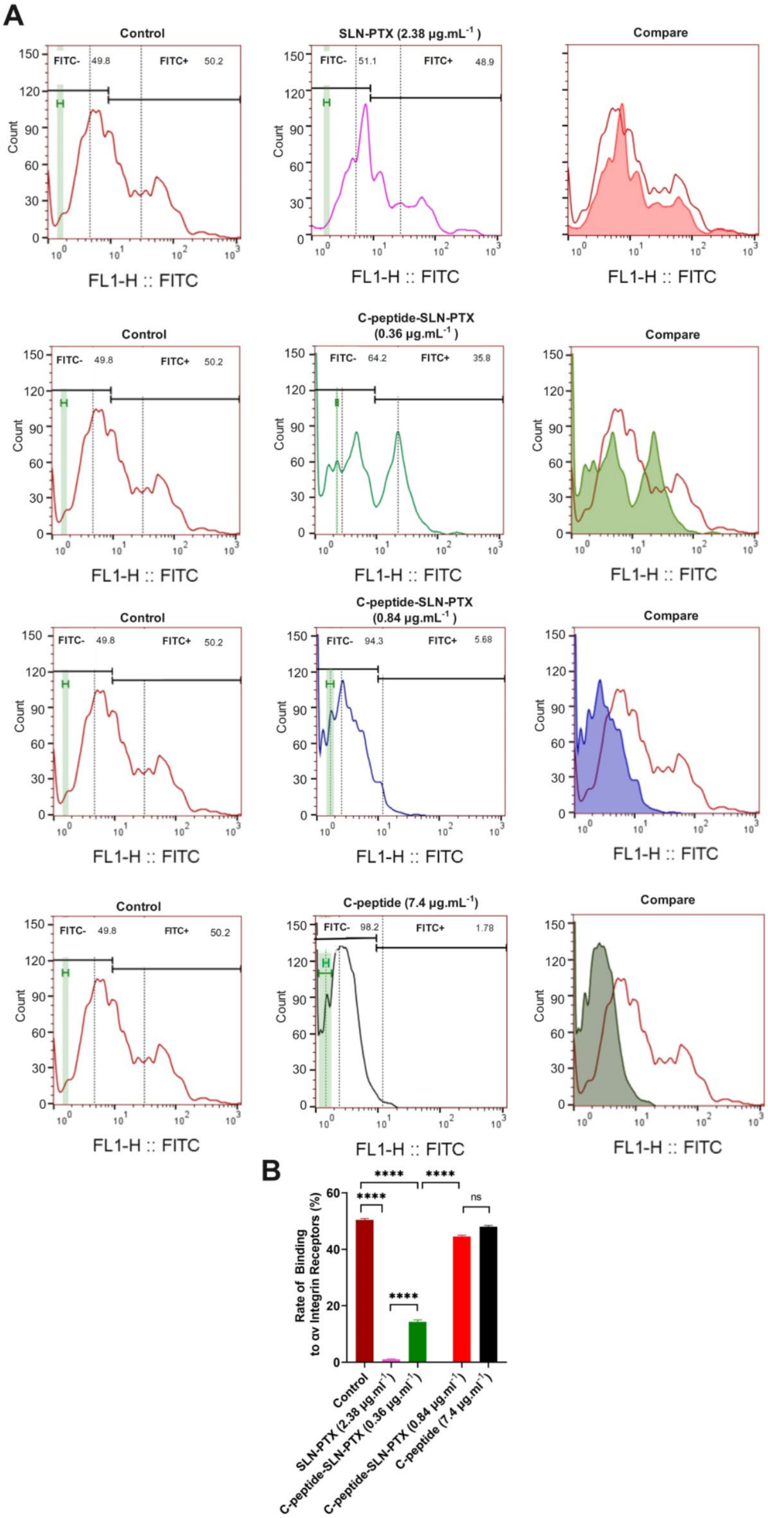

Fig. 6. Receptor-binding assays using flow cytometry. (**A**) 4T1 cells were incubated with control, SLN-PTX (2.38 µg.ml^{-1}), C-peptide-SLN-PTX (0.36 and 0.84 µg.ml^{-1}), and C-peptide (7.4 µg.ml^{-1}). After adding anti-αv integrin antibody and (FITC)-conjugated secondary antibody, flow cytometric analysis was performed. (**B**) Quantitative analysis of the flow cytometry assay using Prism 8 software (two-way ANOVA, mean ± SEM, $n = 3$, ****$P < 0.0001$, ***$P < 0.001$, **$P < 0.01$, *$P < 0.05$, or ns: not significant).

and survival rates were monitored, and liver function and positron emission tomography (PET) imaging were evaluated at the end of the treatment.

At the conclusion of the study, the C-peptide-SLN-PTX group exhibited a significantly smaller average tumor volume of 516 mm^3 compared to the PBS (2828 mm^3, $P < 0.0001$), PTX (1796 mm^3, $P < 0.0001$), and SLN-PTX (997 mm^3, $P = 0.0090$) groups (Fig. 7B). This corresponds to an approximately 82% tumor suppression rate for C-peptide-SLN-PTX, compared to about 68% for SLN-PTX and 36% for PTX (Fig. 7C). Additionally, the mean tumor weight was significantly lower in the C-peptide-SLN-PTX group (0.45 g) compared to the PBS (3.43 g), PTX (2.17 g), and SLN-PTX (1.25 g) groups (Fig. 7D). The C-peptide-SLN-PTX and SLN-PTX treatments improved survival rates to 83.3%, compared to 66.6% for PTX and 50.0% for PBS (Fig. 7E). Mice treated with C-peptide-SLN-PTX also showed better overall health and weight gain (Fig. 7F).

Liver function tests revealed elevated levels of alanine aminotransferase (ALT) and aspartate aminotransferase (AST) in the PBS, PTX, and SLN-PTX groups compared to healthy controls. In contrast, the C-peptide-SLN-PTX group maintained normal ALT and AST levels, indicating reduced hepatic toxicity. These results suggest that C-peptide-SLN-PTX not only enhances tumor suppression but also improves survival rates and reduces hepatic toxicity, making it a promising candidate for further investigation in cancer therapy (Fig. 7G, H).

PET scan

Tumor progression and treatment effectiveness were assessed using 18 F-FDG-PET imaging. On the final day of the treatment period (day 39), the C-peptide-SLN-PTX group exhibited significantly lower tumor uptake compared to the SLN-PTX, PBS, and PTX groups. This observation indicates superior tumor control in the C-peptide-SLN-PTX group relative to all other groups, including SLN-PTX (Fig. 8A). Quantification results showed that the Standardized Uptake Value (SUV) in the SLN-PTX group was significantly lower than in the PTX group, while the SUV in C-peptide-SLN-PTX-treated mice was lower than in all other groups (Fig. 8B). This finding suggests that the metabolic activity of the tumor in the C-peptide-SLN-PTX group is markedly reduced compared to the others, highlighting the enhanced efficacy of the C-peptide-SLN-PTX formulation in controlling tumor growth and activity.

Evaluation of pulmonary metastasis

The evaluation of pulmonary metastasis was conducted by estimating metastatic nodules and performing H&E staining on lung tissues. The results showed that the PBS and PTX groups had 25 ± 3 and 16 ± 2 metastatic nodules, respectively. The SLN-PTX treatment slightly reduced these nodules to 4 ± 1, while no metastatic nodules were observed in the C-peptide-SLN-PTX group (Fig. 9A, B). H&E staining confirmed extensive metastasis in the PBS group, moderate metastasis in the PTX group, minimal metastasis in the SLN-PTX group, and no detectable metastasis in the C-peptide-SLN-PTX group (Fig. 9C). The tumor masses in the C-peptide-SLN-PTX group were significantly smaller (57.34%) compared to the other groups: PBS (93.46%), PTX (80.23%), and SLN-PTX (70.12%). In pre-treatment mice, the tumor mass was 48.32% (Fig. 9D, E).

The enhanced tumor suppression observed with C-peptide-SLN-PTX is likely due to the synergistic effects of targeted delivery and controlled drug release. The C-peptide decoration on SLNs facilitates targeted binding to $\alpha v\beta 3$ integrin receptors, which are overexpressed in tumor and endothelial cells, enhancing the accumulation of the therapeutic agent at the tumor site.

This targeted approach not only improves the efficacy of paclitaxel but also minimizes systemic toxicity, as evidenced by the normalized liver enzyme levels in the treatment group. The pH-sensitive release profile ensures that the drug is predominantly released in the acidic microenvironment of the tumor. This study successfully developed and characterized a multifunctional theranostic platform based on integrin-targeted SLNs for the treatment of TNBC.

Immunohistochemical analyses

To further elucidate the antitumor mechanisms of PTX, SLN-PTX, and C-peptide-SLN-PTX, we examined the immunohistochemical markers Ki-67, Bcl-2, and p53 in tumor tissues from each group on the last day of administration (day 39). Ki-67 staining, which serves as a proliferative index, revealed significant differences in cell proliferation between the treated groups and the PBS control group. The PBS group exhibited markedly high Ki-67 expression, indicating robust growth and proliferation of tumor cells. In contrast, we observed a considerable decrease in Ki-67 expression in the treated groups, with the most substantial reduction occurring in the C-peptide-SLN-PTX group. Specifically, the results showed that 55% of cells were Ki-67 positive in the PBS group, compared to 42% for PTX, 30% for SLN-PTX, and just 5% for C-peptide-SLN-PTX. Additionally, Bcl-2 and p53 staining were performed to assess apoptosis in tumor tissues. Notably, C-peptide-SLN-PTX treatment resulted in a significant decrease in Bcl-2 (the anti-apoptotic marker) expression compared to the control and other treatment groups. The percentages of Bcl_2 positive cells were 97% for PBS, 72% for PTX, 42% for SLN-PTX, and only 7% for C-peptide-SLN-PTX treated groups. The proportion of p53-positive cells (the pro-apoptotic marker) in all treatment groups was significantly higher than that in the PBS group, with the highest percentage observed in the C-peptide-SLN-PTX group. The percentages of p53-positive cells were 10% for PBS, 33% for PTX, 52% for SLN-PTX, and 92% for C-peptide-SLN-PTX treated groups. These findings suggest that C-peptide-SLN-PTX exhibits a superior antitumor effect by significantly inhibiting cell proliferation and promoting apoptosis compared to other treatment modalities. This enhanced effectiveness is attributed to the tumor-targeting properties of the peptide, which allows for more precise delivery and action against cancer cells (Fig. 10).

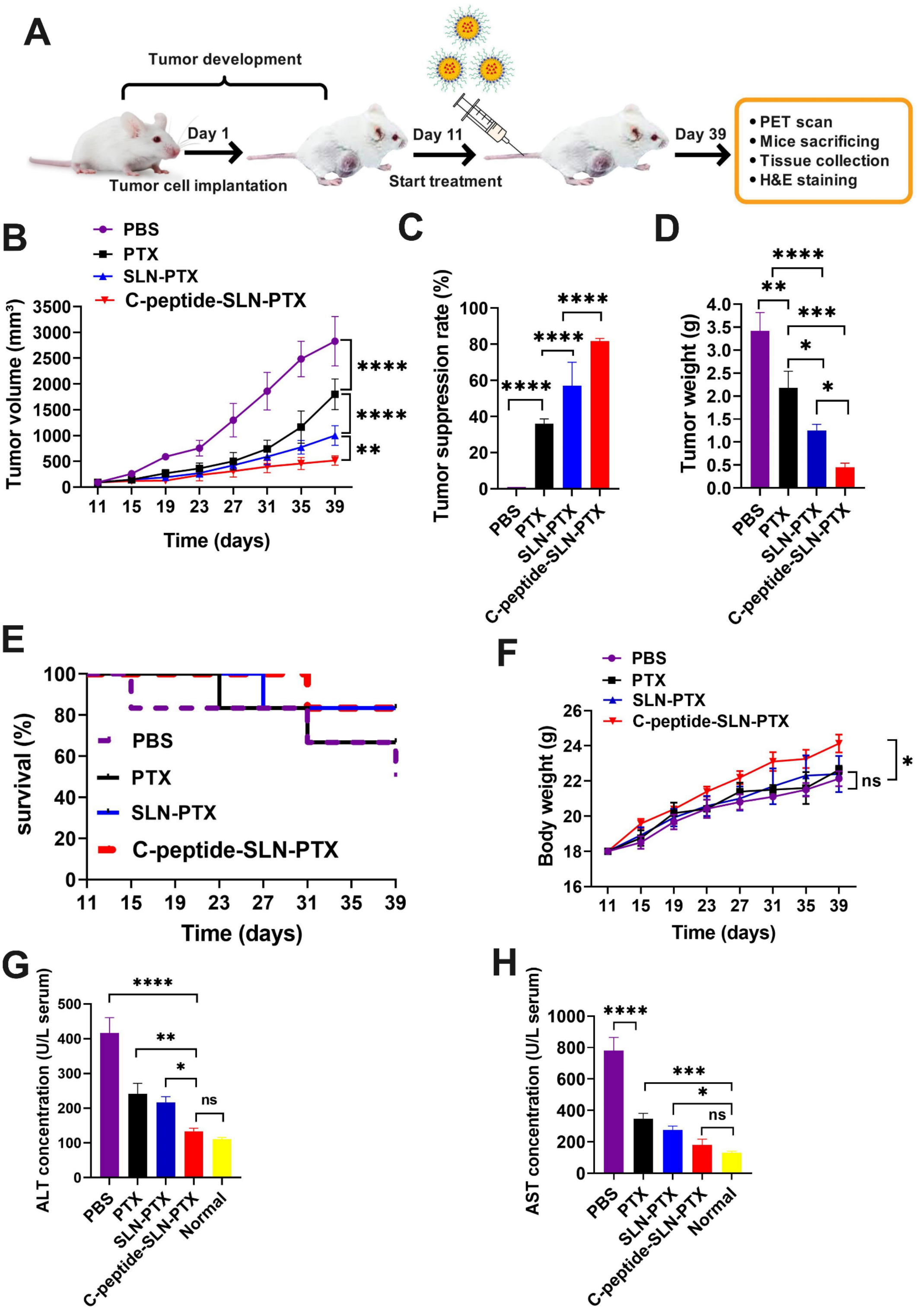

Fig. 7. Antitumor efficacy analysis. **(A)** An overview diagram of the therapeutic protocols applied in the study. (**B**) Tumor volumes across different treatment groups ($n = 6$ mice per group) were analyzed with two-way ANOVA performed through Prism software. (**C**) Tumor suppression rates post-treatment for each group ($n = 6$ mice per group), analyzed using Prism software with one-way ANOVA. (**D**) Average tumor weights in various treatment groups ($n = 6$ mice per group), analyzed using Prism software with one-way ANOVA. (**E**) Survival rates of mice in each group following treatment, analyzed using Prism software with one-way ANOVA ($n = 6$ mice per group). (**F**) Body weight measurements of each treatment group were taken every 4 days until day 39($n = 6$ mice/group), and analysis was done by prism software (two-way ANOVA). Assessment of liver enzyme activity of each treated mice group at day 39, **G**: alanine aminotransferase (ALT) and (**H**) aspartate aminotransferase (AST), analysis was done by prism software (two-way ANOVA, $n = 6$, mean ± SEM $^{****}P < 000.1$, $^{***}P = 0.0006$, $^{**}P = 0.0037$, $^{*}P = 0.0260$ and ns = not significant.

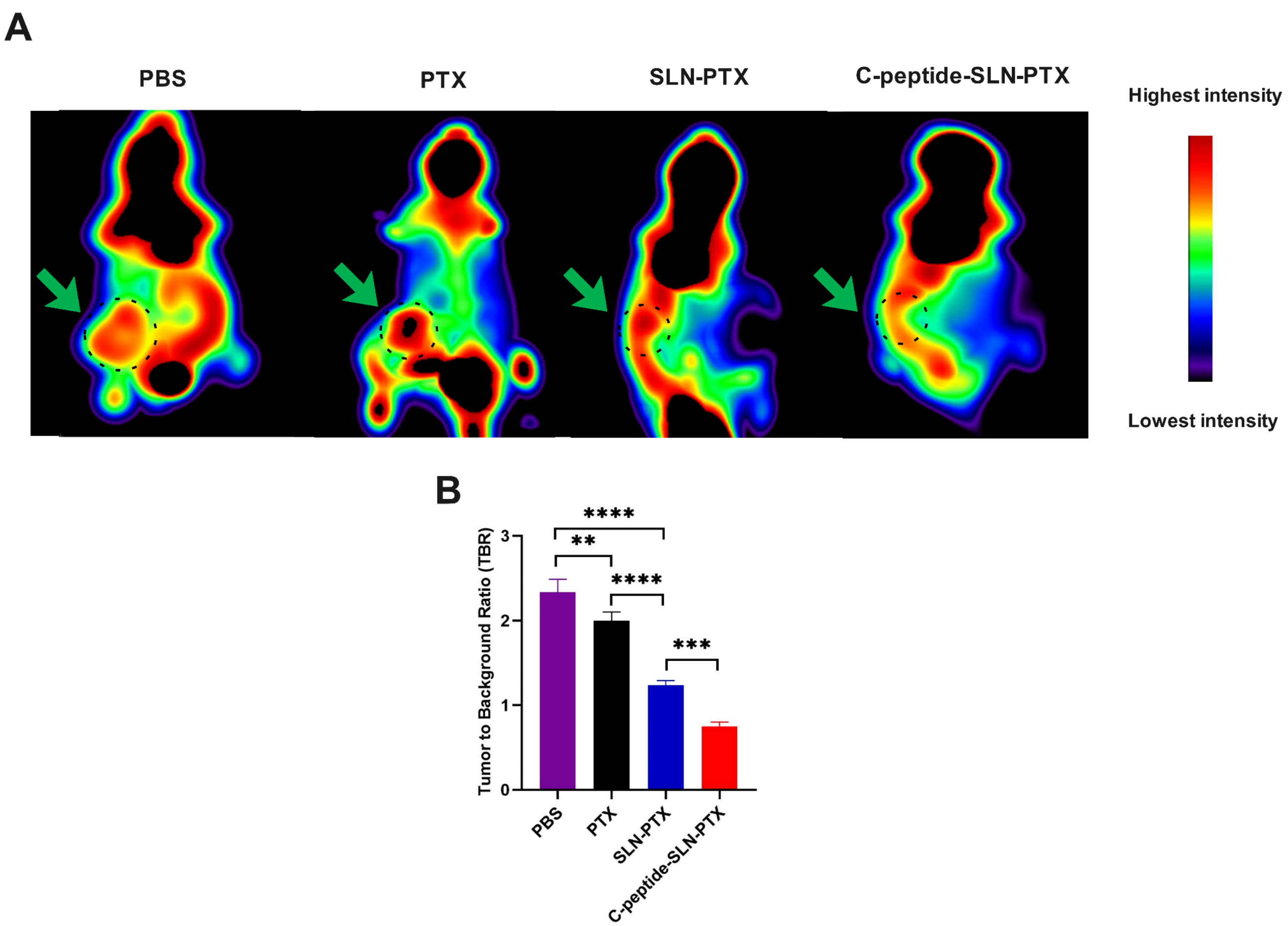

Fig. 8. BALB/c Mouse PET Scan and Image Analysis. (**A**) Animal PET Imaging. (**B**) Tumor-to-Background Ratio (TBR) Analysis. Quantitative calculation of TBR was performed using VivoQuant software and analyzed by one-way ANOVA with Prism software (mean ± SEM, ****$P < 0.001$, ***$P = 0.0006$,**$P = 0.0083$, *$P = 0.0037$, $P = 0.0260$, and ns = not significant).

Materials and methods

Materials

The study utilized a range of materials, including stearic acid, Precirol ATO 5, Poloxamer 407, soybean lecithin, and paclitaxel, all sourced from Sigma-Aldrich. Additionally, MTT reagent (3-(4,5-dimethylthiazol-2-yl)-2,5-diphenyltetrazolium bromide), 1-Ethyl-3-[3-dimethylaminopropyl] carbodiimide hydrochloride (EDC), and N-hydroxysuccinimide (NHS) were employed. Cellular studies were conducted using RPMI-1640 medium, penicillin, streptomycin, fetal bovine serum (FBS), and trypsin-EDTA, all provided by Gibco. The anti-integrin alpha v antibody was obtained from Abcam, and, fluorescein (FITC)-conjugated AffiniPure™ F(ab')2 Fragment Donkey Anti-Rabbit IgG (H + L) was acquired from Jackson ImmunoResearch Laboratories. The murine 4T1 mammary carcinoma cell line was sourced from the Pasteur Institute in Tehran, Iran. Female athymic BALB/c mice, aged 4–6 weeks, were provided from the Institute of Biochemistry and Biophysics (IBB) at the University of Tehran, Tehran, Iran.

Synthesis of nanoparticles

Preparation of SLNs

SLNs were synthesized using a hot homogenization technique followed by ultrasonication. Initially, the lipid phase was prepared by melting 90 mg of stearic acid and 20 mg of Precirol at 80 °C, to which 10 µl of Tween 20 was added. Concurrently, the aqueous phase was prepared by dispersing 70 mg of lecithin in 3 mL of deionized water, followed by sonication at 70 W for 10 min at 80 °C. Afterward, 80 mg of Poloxamer 407 was incorporated into the lecithin dispersion and stirred for 5 min at 80 °C. The aqueous phase was then gradually added to the lipid phase at 80 °C using a homogenizer set to 12,000 rpm for 15 min. The resulting mixture was sonicated for an additional 10 min at 70 W, dispersed in 2 mL of distilled water, and sonicated for 15 min at 4 °C. The solution was stored at 4 °C for 24 h to facilitate SLN formation. The final mixture was centrifuged at 14,000 rpm for 20 min, and the resulting pellets were re-dispersed in fresh deionized water. This procedure was adapted from previous studies with modifications[44,45].

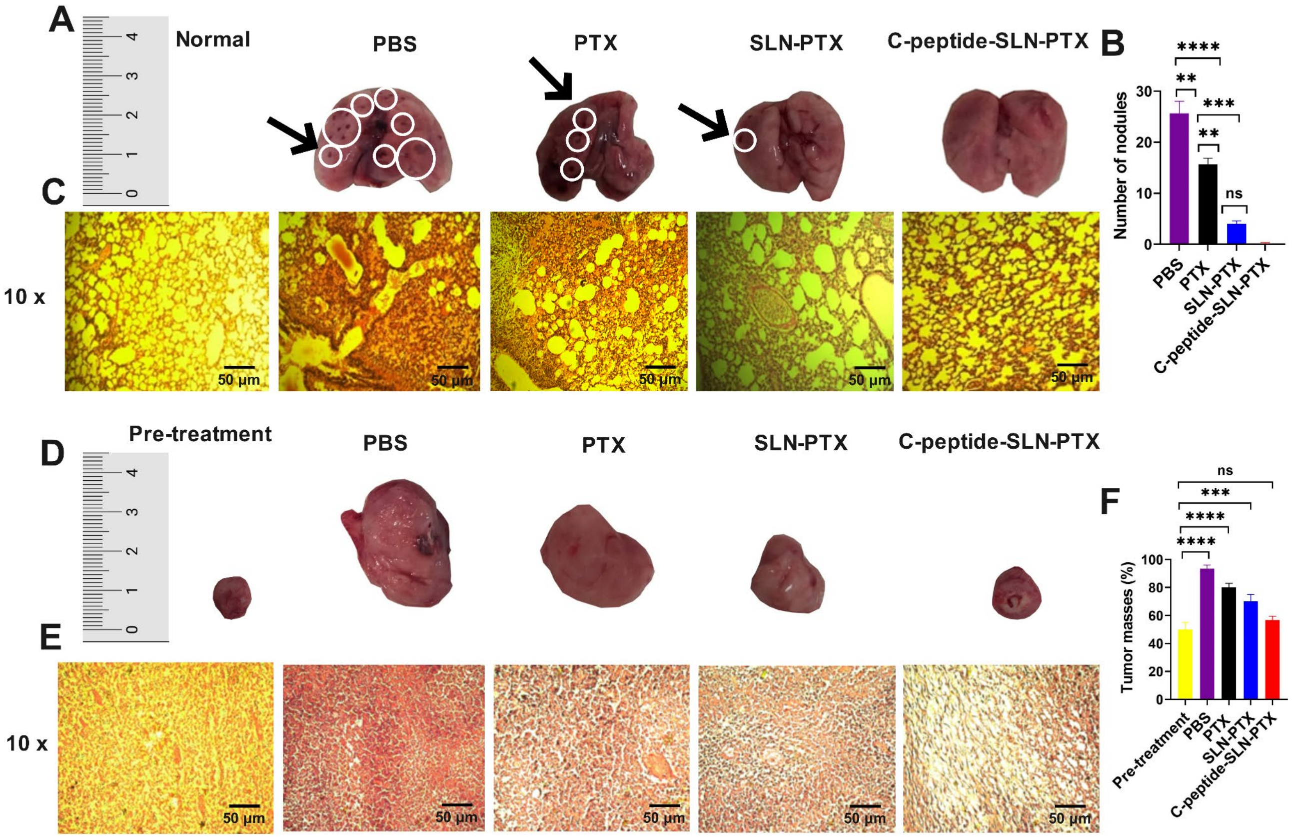

Fig. 9. Lung metastasis and tumor masses investigation. (**A**) Digital photos of harvested lungs from each group to evaluate metastatic nodules. (**B**) visible metastatic nodules analyzed by one-way ANOVA using prism software ($n = 6$ mice per group). (**C**) H&E staining of lung tissues. (**D**) Digital photos of harvested tumors from each group. (**E**) H&E staining of tumor tissues harvested from each group ($n = 6$ mice per group). (**F**) The H&E stained tumor tissue images were submitted to ImageJ software, and the tumor masses were measured. The measurements were then analyzed by one-way ANOVA using Prism software. mean ± SEM, ****$P < 000.1$, ***$P = 0.0006$, **$P = 0.0037$, ns = not significant.

Fabrication of paclitaxel-loaded SLN (SLN-PTX)

The fabrication of paclitaxel-loaded SLNs (SLN-PTX) followed a similar methodology to that of blank SLNs, with the key difference being the addition of 3 mg of paclitaxel powder dissolved in 200 µl of absolute ethanol to the lipid phase before the aqueous phase was incorporated. After 24 h of incubation at 4 °C, the suspension was centrifuged, and the supernatant was discarded to isolate the nanoparticles from excess lipids and unencapsulated PTX.

Peptide synthesis

The C-peptide ($_2$HN-SDPNGRRLTESYCETWRTEAPSSCHHAYIV-COOH) was synthesized using a standard Fmoc solid-phase peptide synthesis protocol on a 2-CTC resin with a loading capacity of 1.0 mmol/g. Sequential coupling of Fmoc-protected amino acids was performed in anhydrous DMF using DIEA and HCTU. After each coupling, the resin was washed with DMF, DCM, and methanol. The Fmoc groups were removed with a 20% piperidine solution in DMF. To cleave the peptide from the resin, a TFA cleavage mixture (TFA/tris(isopropylsilyl) ether/water, 95:2.5:2.5, v/v/v) was used. Purification involved RP-HPLC on a preparative C18 column with a gradient of acetonitrile and water containing 0.1% TFA. Peptide purity exceeding 95% was confirmed via analytical RP-HPLC on a C18 column, and molecular weight was verified using electrospray ionization LC-MS. Additional details can be found in the Supplementary Information (Figures S1, S2). Disulfide bond formation in the synthesized C-peptide was confirmed by the Ellman assay. C-peptide (1.3 µM) was added to the 100 mM sodium phosphate reaction buffer at pH 8.0 containing 100 mM EDTA. Next, the Ellman reagent [4 mg/ml of DTNB (5,5'-dithiobis-(2-nitrobenzoic acid))] was prepared. The reaction was started by mixing the sample solution with an equal volume of the Ellman's reagent. After 15 min incubation at room temperature, the sulfhydryl concentration was calculated by reading the absorbance of reaction at 412 nm ($\varepsilon = 1.36 \times 104$ M − 1 cm − 1) versus a sulfhydryl standard 'cysteine' treated in the same manner by using a UV-visible spectrophotometer.

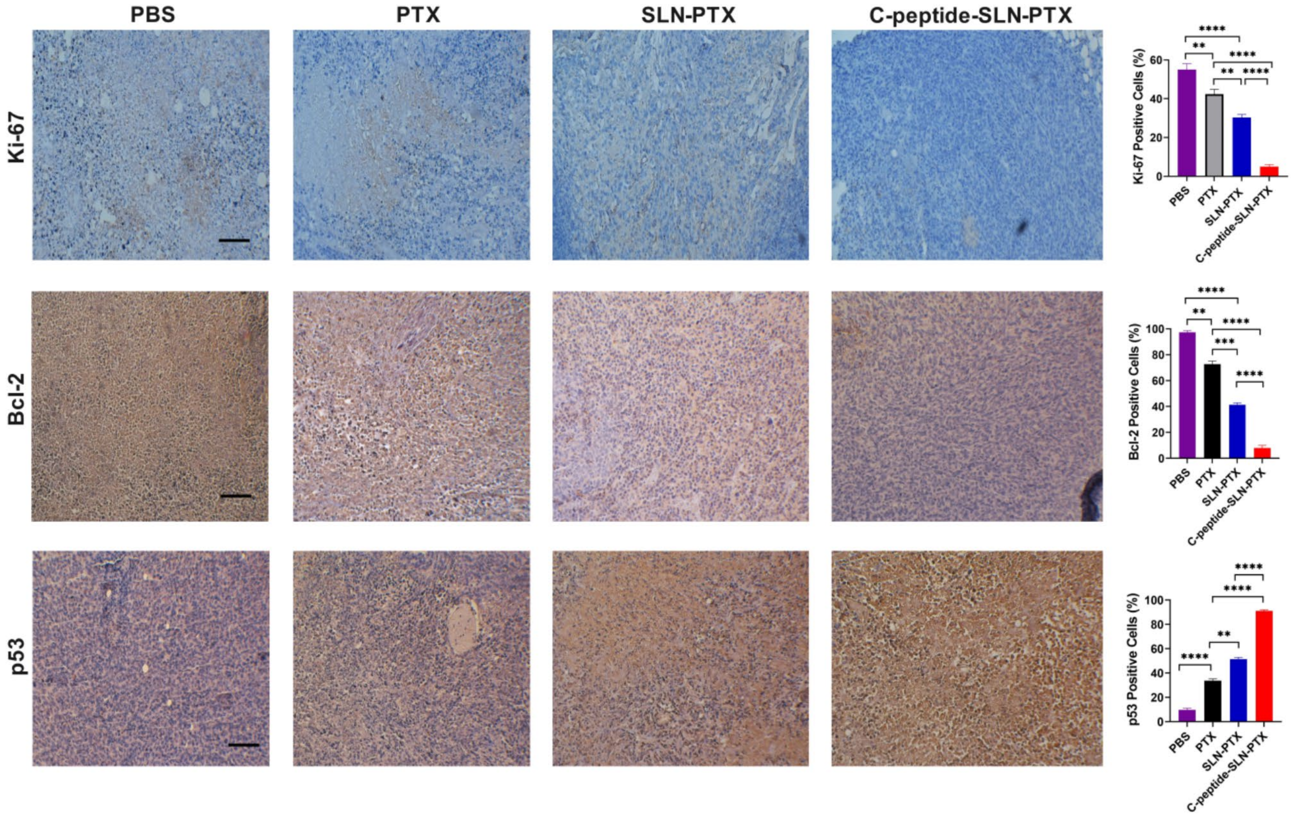

Fig. 10. The impact of treatments (PBS, PTX, SLN-PTX and C-peptide-SLN-PTX) on tumor growth, metastasis, and associated signaling pathways in vivo. Representative images of immunohistochemical analyses and quantitative assessments of Ki-67, Bcl-2, and p53 staining for each treated mice group (Magnification 40×; bar = 20 µm). Data were quantified using ImageJ software and analyzed with Prism software (mean ± SEM, $n = 3$, $^{****}P < 000.1$, $^{***}P = 0.0006$, $^{**}P = 0.0037$, ns = not significant).

Preparation of peptide-conjugated SLNs (C-peptide-SLNs)

SLNs were functionalized with C-peptide through an acid-amine coupling reaction. Initially, SLNs (10 mg/ml) were suspended in a phosphate buffer (pH 7.4) with EDC (15 mg/ml) and NHS (10 mg/ml) to activate the carboxyl groups on the SLNs. After thorough mixing using a vortex for 5 min, The freeze-dried C-peptide (1 mg/ml) was added, and the mixture was incubated for 8 h at room temperature, and shaken gently at 80 rpm. Post-reaction purification involved centrifugation to remove unbound reagents, thereby producing functionalized C-peptide-SLNs ready for enhanced targeted therapy applications.

In Vitro physicochemical characterization of nanoparticles

Measurement of hydrodynamic diameter (HD), polydispersity index (PDI), and Zeta potential

Dynamic light scattering (DLS, model: Micro Trac– Nano Flex) was employed to evaluate the average particle size, PDI, and zeta potential of nanoformulations. The formulations were diluted in distilled water, and each measurement was performed thrice. The storage stability of the nanoparticles was assessed through freeze-drying and storage at -20 °C, with evaluations for mean HD, PDI, and zeta potential conducted after 4 months.

Serum stability of nanoparticles

The stability of the nanoparticles in the blood serum of BALB/c mice was investigated to simulate their persistence within a biological environment. The SLN suspension was mixed with mouse blood serum and incubated at 37 °C for various time intervals, after which mean HD and PDI were measured using DLS.

Fourier transform infrared spectroscopy (FTIR) analysis

FTIR (JASCO 4700) was performed to determine the functional groups and possible interactions within the components of the nanocomplex. Samples were mixed with KBr, compressed into pellets, and analyzed over a range of 4000 to 400 cm^{-1}.

Thermal analysis (DSC/TGA)

Thermal stability was evaluated using Differential Scanning Calorimetry (DSC) and Thermogravimetric Analysis (TGA). TGA, conducted with a THERMO NIKOLED analyzer, scanned from 0 to 400 °C at a heating rate of

10 °C/min under a nitrogen atmosphere. DSC (Agilent 7890 A) recorded the heat flow and melting endotherm characteristics. Each sample (4 mg) was subject to identical temperature range and conditions.

X-ray diffraction measurement (XRD)

The crystal structures and phase compositions of the nanoparticles were studied through XRD (Inel, EQUINOX3000, France), gathering data within the angle range of 20–100° (2θ).

UV-visible spectroscopy analysis

UV-visible spectroscopy (Varian, Carry 100 Bio, Australia) was conducted to confirm the functionalization of nanoparticles with the peptide.

Circular dichroism (CD) spectroscopy evaluation

The secondary structure of the peptide was analyzed pre- and post-interaction with the nanoparticles using Circular Dichroism (CD) on an Aviv 215 instrument.

Morphological analysis

Field Emission Scanning Electron Microscopy (FESEM, TESCAN, MIRA3) and Atomic Force Microscopy (AFM, Brisk, Arapajuhesh, Iran) were utilized to assess the size and morphology of the nanoparticles.

Calibration curve of PTX

For PTX quantification, a calibration curve was created by dissolving 1 mg of PTX in absolute ethanol and preparing serial dilutions in phosphate buffer. Absorbance was measured, leading to the plot of the standard curve.

Assessment of encapsulation efficiency

The encapsulation efficiency (EE%) of PTX within SLNs was calculated via UV-Vis spectrophotometry. Free PTX was separated by centrifugation, and its concentration was compared against the calibration curve to derive EE%.

$$\text{Encapsulation Efficiency (\%)} = \frac{Total\ PTX\ added - Free\ PTX\ in\ suspansion}{Total\ PTX\ added} \times\ 100$$

Drug release analysis

The drug release profile was studied using a dialysis bag method. PTX, SLN-PTX, and peptide-SLN-PTX suspensions (1 ml each) were enclosed in dialysis bags (Sigma) with a 12 kDa molecular weight cut-off. These were immersed in 25 ml of phosphate-buffered saline (PBS) at pH levels of 4.7, 5.5, 6, 6.5, 7.4 and 8.5, incubated in a sealed container at 37 °C under continuous shaking (100 rpm). Samples were withdrawn at specific intervals for concentration analysis with the removed volume replaced, and PTX concentrations quantified using UV-visible spectroscopy across 190–800 nm.

Cell culture experiments

In vitro cytotoxicity assay

Murine 4T1 mammary carcinoma tumor (MCT) and MDA-MB-231 (M D Anderson - Metastatic Breast – 231) cell lines were cultured in RPMI-1640 medium augmented with 10% FBS and 1% penicillin at 37 °C and 5% CO_2. Cytotoxicity was evaluated through a colorimetric MTT assay. When cells reached 90% confluence, a trypsin-EDTA solution (700 µl) was used to detach them. Post-centrifugation, cells were resuspended in medium with 10% serum, seeded at 10,000–15,000 cells/well in a 96-well plate, and incubated overnight. The medium was then replaced with fresh media containing varying concentrations of treatments for 24 h. MTT powder (5 mg/ml) prepared in PBS was added at 10 µl per well, and the cells were incubated at 37 °C for 4 h. Following this, 100 µl of DMSO was added to dissolve formazan crystals and mixed thoroughly. Absorbance was recorded at 595 nm, with untreated cells serving as the control for 100% viability. The IC_{50} value was calculated via curve-fitting of cell viability data.

Scratch assay

The scratch assay was employed to evaluate cell migration. Approximately 200,000 cells were seeded in a 24-well plate and incubated for 24 h at 37 °C with 5% CO_2 until confluent. After removing the media and washing with PBS, a scratch was created in each well using a sterile pipette tip. Wells were treated with PTX, C-peptide, and nanoparticle formulations at 70% of the IC_{50} concentration in supplemented media for 24 and 48 h. Control wells received media only. The initial and follow-up scratches were imaged with an inverted microscope to quantify migration using ImageJ analysis software.

Exploring peptide-conjugated nanoparticles' affinity for $\alpha_v$integrin receptors

The binding ability of peptide-bound nanoparticles to αv integrin receptors was evaluated through flow cytometry. First, 4T1 cultured cells were collected, centrifuged, and resuspended in fresh medium containing 10% FBS. Each well of a 12-well plate was then populated with 500,000 cells and subjected to various treatments, including a control group (no treatment), SLN-PTX at 2.38 µg/mL, C-peptide-SLN-PTX at both 30% and 70% doses of IC50 (0.36 and 0.84 µg/mL, respectively), C-peptide at 70% of the IC50 dose (7.4 µg/mL), and a constant dose of anti-integrin alpha v antibody. Following a 3-hour incubation period, an equal volume of FITC-labeled secondary antibody was added to each well and allowed to interact with the cells for an additional hour.

After this interaction, the cellular contents were centrifuged to remove any unbound probes and subsequently resuspended in fresh medium for analysis. The interactions were then assessed using flow cytometry to determine the binding efficiency of the peptide-bound nanoparticles to the αv integrin receptors[46,47]. Magnetic Resonance Imaging (MRI) was also utilized to assess the binding affinity of C-peptide-conjugated SLN-PTX to integrin receptors on breast tumor cells. Iron oxide nanoparticles (Fe_3O_4) were encapsulated in the peptide-conjugated carriers to enhance imaging contrast. A competitive binding assay was executed using an anti-integrin-alpha v antibody (antiαvβ). The 4T1 cell line (500,000 cells/well) was incubated with the nanoparticles (70% of IC_{50} concentration) and anti-integrin alpha v antibody (at concentrations of 100, 200, and 300 ng/ml) for four hours. Post-incubation, cells were washed to remove unbound nanoparticles, and MRI imaging was performed for visual analysis.

In vivo experiments

Evaluation of antitumor activity

Twenty-four female BALB/c mice, aged 4–6 weeks, were sourced from the Animal Core Facility at the Institute of Biochemistry and Biophysics, University of Tehran. All procedures adhered to ethical standards set by the University of Tehran's Ethics Committee for Animal Research, receiving approval from the Biomedical Research Ethics Committee of the University of Guilan (IR.GUILAN.REC.1401.010). All methods were performed in accordance with the relevant guidelines and regulations. A total of 10^5 murine 4T1 MCT cells in 50 µl were injected into the right flanks of mice. Once tumors reached ~ 100 mm^3, they were excised from cancerous mice and transplanted into new BALB/c mice. The implantation was performed under anesthesia using ketamine (100 mg/k, i.p) and xylazine (10 mg/kg, i.p). Mice were divided into four treatment groups (6 mice/group): control (PBS), PTX (administered with Cremophor EL), SLN-PTX, and C-peptide-SLN-PTX, administered intravenously at a dose of 5 mg/kg PTX every 4 days. Tumor dimensions and mouse weight were monitored bi-weekly using calipers. Tumor volumes were calculated using the formula: $V = \text{length (cm)} \times \text{width}^2\ (\text{cm}^2) \times 0.5$. Mice selected for positron emission tomography (PET) imaging based on average tumor sizes were euthanized with CO_2 (20% of the cage volume per minute) on day 39 for histological analysis.

PET scan

On the final treatment day, one mouse from each group was selected for imaging. Following an eight-hour fasting period, mice were anesthetized and administered 0.4 mCi of 2-deoxy-2-[^{18}F] fluoro-D-glucose (FDG) via the tail vein. A PET scan assessed tumors to monitor treatment effectiveness.

Quantitative calculation of Tumor-to-background ratio (TBR)

The TBR from PET scans was analyzed to assess tumor metabolic activity and differentiate tumor progression from treatment-related changes. The TBR was quantified through mean uptake calculations of tumor and background regions, employing VivoQuant software for image data processing[48]. The TBR was determined using the following formula:

$$\text{TBR} = \frac{\text{Mean Tumor Update}}{\text{Mean Background Update}}$$

Ex vivo studies

Histochemistry staining

Histopathological examinations of tumor and lung sections from treatment groups were conducted at study completion using H&E staining. Tissues were preserved in 10% paraformaldehyde for evaluation. Stained tissues were observed under an inverted fluorescence microscope (TS100, Nikon, Japan).

Assessment of liver enzyme activity

Blood samples were collected for ALT analysis using the ALT/GPT detection method to assess liver function in each group. Sera were separated via centrifugation at 4000 rpm for 10 min.

Immunohistochemistry staining

Tumor tissues were harvested from each group at the end of the treatment period, and immunohistochemical (IHC) staining analysis was performed to localize specific tissue antigens, including Ki-67, Bcl-2 and p53.

Statistical analysis

Data analysis, graph generation, and statistical evaluation were performed using GraphPad Prism software (version 8.0.2), presenting results as mean ± SEM. One-way ANOVA followed by Tukey's post hoc test was used for multiple groups with one independent variable, or two-way ANOVA for cases with two independent variables. Statistical significance was assessed at a confidence level of 95% ($P < 0.05$), with image quantification conducted using ImageJ software and PET images analyzed using RadiAnt DICOM Viewer.

Conclusion

This study successfully developed and comprehensively characterized peptide-decorated SLNs targeting $\alpha v\beta_3$ integrins, which are highly expressed in TNBC. The nanoparticles demonstrated stability over time, appropriate size and morphology, uniform distribution, and high encapsulation efficiency of approximately 90%. They exhibited a sustained release pattern of PTX, lasting around 90 h, ensuring controlled drug delivery in the acidic tumor microenvironment. Notably, the release of PTX was enhanced in acidic conditions (pH 4.7, 5.5, 6 and

6.5), which resemble the tumor microenvironment, compared to physiological pH (pH 7.4), thereby improving drug delivery.

Mechanistically, the C-peptide derived from human endostatin retained its random coil conformation upon conjugation to SLNs, facilitating efficient targeting and binding to αv integrin receptors on TNBC cells. Flow cytometry analysis confirmed that C-peptide-SLN-PTX targets αv integrin receptors in 4T1 cells. In vivo studies demonstrated that C-peptide-SLN-PTX significantly outperformed free PTX and SLN-PTX in tumor suppression, achieving an 82% reduction in tumor volume and preventing pulmonary metastasis. Additionally, results from 18 F-FDG-PET imaging indicated that C-peptide-SLN-PTX had a greater effect on inhibiting tumor growth compared to other treatment groups. This targeted approach not only improved the efficacy of paclitaxel but also minimized systemic toxicity, as evidenced by normalized liver enzyme levels (AST and ALT) and improved survival rates in treated groups, highlighting the nontoxic nature of the formulation. Immunohistochemical analyses demonstrated that C-peptide-SLN-PTX significantly inhibits tumor cell proliferation and promotes apoptosis, as evidenced by Ki-67 positivity at just 5%, Bcl-2 positivity at 7%, and p53 positivity at 92%.

The promising results presented in this study suggest that integrin-targeted SLN-PTX could represent a significant advancement in the precision treatment of TNBC, offering a more effective and less toxic therapeutic option.

Data availability

All data generated or analysed during this study are included in this manuscript (and its Supplementary Information files).

Received: 28 November 2024; Accepted: 10 February 2025

References

1. Wilkinson, L. & Gathani, T. Understanding breast cancer as a global health concern. *Br. J. Radiol.* **95**(1130), 20211033 (2022).
2. Obidiro, O., Battogtokh, G. & Akala, E. O. Triple negative breast cancer treatment options and limitations: future outlook. *Pharmaceutics* **15**(7), 1796 (2023).
3. Yang, R. et al. Therapeutic progress and challenges for triple negative breast cancer: targeted therapy and immunotherapy. *Mol. Biomed.* **3**(1), 8 (2022).
4. Balahura Stămat, L. R. & Dinescu, S. Inhibition of NLRP3 inflammasome contributes to paclitaxel efficacy in triple negative breast cancer treatment. *Sci. Rep.* **14**(1), 24753 (2024).
5. Mohamadianamiri, M. et al. Evaluation of prolactin receptor in Triple negative breast Cancer by immunohistochemistry as a predictive factor: a descriptive Analytic Study. *J. Obstet. Gynecol. Cancer Res.* **8**(1), 29–34 (2022).
6. Weaver, B. A. How Taxol/paclitaxel kills cancer cells. *Mol. Biol. Cell.* **25**(18), 2677–2681 (2014).
7. Sharifi-Rad, J. et al. Paclitaxel: application in modern oncology and nanomedicine-based cancer therapy. *Oxidative Med. Cell. Longev.* **2021**(1), 3687700 (2021).
8. Vicari, L. et al. Paclitaxel loading in PLGA nanospheres affected the in vitro drug cell accumulation and antiproliferative activity. *BMC cancer*. **8**, 1–11 (2008).
9. Vismara, E. et al. Albumin and hyaluronic acid-coated superparamagnetic iron oxide nanoparticles loaded with paclitaxel for biomedical applications. *Molecules* **22**(7), 1030 (2017).
10. Lugert, S. et al. Cellular effects of paclitaxel-loaded iron oxide nanoparticles on breast cancer using different 2D and 3D cell culture models. *Int. J. Nanomed.* 161–180 (2019).
11. Qu, N. et al. Docetaxel-loaded human serum albumin (HSA) nanoparticles: synthesis, characterization, and evaluation. *Biomed. Eng. Online*. **18**, 1–14 (2019).
12. Mejia Peña, C. et al. Metronomic and single high-dose paclitaxel treatments produce distinct heterogenous chemoresistant cancer cell populations. *Sci. Rep.* **13**(1), 19232 (2023).
13. Zhang, L. & Zhang, N. How nanotechnology can enhance docetaxel therapy. *Int. J. Nanomed.* 2927–2941 (2013).
14. Luo, K. et al. Co-delivery of paclitaxel and STAT3 siRNA by a multifunctional nanocomplex for targeted treatment of metastatic breast cancer. *Acta Biomater.* **134**, 649–663 (2021).
15. Zheng, Q. et al. A retrospect study based on real-world data to observe metabolic function in cancer patients using albumin-bound paclitaxel. *Sci. Rep.* **13**(1), 9028 (2023).
16. Smith, T. et al. Application of smart solid lipid nanoparticles to enhance the efficacy of 5-fluorouracil in the treatment of colorectal cancer. *Sci. Rep.* **10**(1), 16989 (2020).
17. Yeo, S. et al. Improved anticancer efficacy of methyl pyropheophorbide-a–incorporated solid lipid nanoparticles in photodynamic therapy. *Sci. Rep.* **13**(1), 7391 (2023).
18. da Rocha, M. C. O. et al. Docetaxel-loaded solid lipid nanoparticles prevent tumor growth and lung metastasis of 4T1 murine mammary carcinoma cells. *J. Nanobiotechnol.* **18**, 1–20 (2020).
19. Pawar, H. et al. Folic acid functionalized long-circulating co-encapsulated docetaxel and curcumin solid lipid nanoparticles: in vitro evaluation, pharmacokinetic and biodistribution in rats. *Drug Deliv.* **23**(4), 1453–1468 (2016).
20. Emami, A., Ghafouri, H. & Sariri, R. Polyphyllin D-loaded solid lipid nanoparticles for breast cancer: synthesis, characterization, in vitro, and in vivo studies. *Int. J. Pharm.* **639**, 122976 (2023).
21. Garanti, T., Alhnan, M. A. & Wan, K. W. RGD-decorated solid lipid nanoparticles enhance tumor targeting, penetration and anticancer effect of asiatic acid. *Nanomedicine* **15**(16), 1567–1583 (2020).
22. Zheng, X. C. et al. The theranostic efficiency of tumor-specific, pH-responsive, peptide-modified, liposome-containing paclitaxel and superparamagnetic iron oxide nanoparticles. *Int. J. Nanomed.* 1495–1504 (2018).
23. Banerjee, I. et al. Paclitaxel-loaded solid lipid nanoparticles modified with tyr-3-octreotide for enhanced anti-angiogenic and anti-glioma therapy. *Acta Biomater.* **38**, 69–81 (2016).
24. Ehtesham, S. et al. Functional studies on a Novel Engineered peptide derived from C-Terminal of human endostatin. *Biomacromolecular J.* **4**(1), 58–64 (2018).
25. Li, D. et al. Integrin αvβ6-targeted MR molecular imaging of breast cancer in a xenograft mouse model. *Cancer Imaging*. **21**(1), 44 (2021).
26. Xiao, K. et al. The effect of surface charge on in vivo biodistribution of PEG-oligocholic acid based micellar nanoparticles. *Biomaterials* **32**(13), 3435–3446 (2011).
27. Patel, M. N. et al. Characterization and evaluation of 5-fluorouracil-loaded solid lipid nanoparticles prepared via a temperature-modulated solidification technique. *Aaps Pharmscitech*. **15**, 1498–1508 (2014).

28. Mohseni, R. et al. Oral administration of resveratrol-loaded solid lipid nanoparticle improves insulin resistance through targeting expression of SNARE proteins in adipose and muscle tissue in rats with type 2 diabetes. *Nanoscale Res. Lett.* **14**, 1–9 (2019).
29. Martins, K. F. et al. Preparation and characterization of paclitaxel-loaded PLDLA microspheres. *Mater. Res.* **17**, 650–656 (2014).
30. Keivani Nahr, F. et al. The colloidal and release properties of cardamom oil encapsulated nanostructured lipid carrier. *J. Dispers. Sci. Technol.* **42**(1), 1–9 (2020).
31. Wang, W. W. et al. *Curcumin-loaded solid lipid nanoparticles enhanced anticancer efficiency in breast cancer* (2018).
32. Zanjanchi, P. et al. Conjugation of VEGFR1/R2-targeting peptide with gold nanoparticles to enhance antiangiogenic and antitumoral activity. *J. Nanobiotechnol.* **20**(1), 7 (2022).
33. Vijayakumar, A. et al. Quercetin-loaded solid lipid nanoparticle dispersion with improved physicochemical properties and cellular uptake. *Aaps Pharmscitech.* **18**, 875–883 (2017).
34. Hosseini, S. M. et al. Doxycycline-encapsulated solid lipid nanoparticles as promising tool against Brucella melitensis enclosed in macrophage: a pharmacodynamics study on J774A. 1 cell line. *Antimicrob. Resist. Infect. Control.* **8**, 1–12 (2019).
35. Choi, S. G. et al. Thermosensitive and mucoadhesive sol-gel composites of paclitaxel/dimethyl-β-cyclodextrin for buccal delivery. *PLoS One.* **9**(10), e109090 (2014).
36. Yu, K. et al. Role of four different kinds of polyethylenimines (PEIs) in preparation of polymeric lipid nanoparticles and their anticancer activity study. *J. Cancer.* **7**(7), 872 (2016).
37. Mathew, A. et al. Curcumin loaded-PLGA nanoparticles conjugated with Tet-1 peptide for potential use in Alzheimer's disease. *PLoS One.* **7**(3), e32616 (2012).
38. Liu, K. et al. Paclitaxel and quercetin nanoparticles co-loaded in microspheres to prolong retention time for pulmonary drug delivery. *Int. J. Nanomed.* 8239–8255 (2017).
39. Wang, Y. et al. Targeted delivery of quercetin by nanoparticles based on chitosan sensitizing paclitaxel-resistant lung cancer cells to paclitaxel. *Mater. Sci. Eng. C.* **119**, 111442 (2021).
40. Kievit, F. M. et al. Doxorubicin loaded iron oxide nanoparticles overcome multidrug resistance in cancer in vitro. *J. Controlled Release.* **152**(1), 76–83 (2011).
41. Gao, S. et al. Nanocatalytic tumor therapy by biomimetic dual inorganic nanozyme-catalyzed cascade reaction. *Adv. Sci.* **6**(3), 1801733 (2019).
42. Chen, H. H. et al. pH-Responsive therapeutic solid lipid nanoparticles for reducing P-glycoprotein-mediated drug efflux of multidrug resistant cancer cells. *Int. J. Nanomed.* 5035–5048 (2015).
43. Lazzari, S. et al. Colloidal stability of polymeric nanoparticles in biological fluids. *J. Nanopart. Res.* **14**, 1–10 (2012).
44. Baek, J. S. & Cho, C. W. Controlled release and reversal of multidrug resistance by co-encapsulation of paclitaxel and verapamil in solid lipid nanoparticles. *Int. J. Pharm.* **478**(2), 617–624 (2015).
45. Girotra, P. & Singh, S. K. Multivariate optimization of Rizatriptan benzoate-loaded solid lipid nanoparticles for brain targeting and migraine management. *AAPS PharmSciTech.* **18**(2), 517–528 (2017).
46. Assareh, E. et al. A cyclic peptide reproducing the α1 helix of VEGF-B binds to VEGFR-1 and VEGFR-2 and inhibits angiogenesis and tumor growth. *Biochem. J.* **476**(4), 645–663 (2019).
47. Farzaneh Behelgardi, M. et al. A peptide mimicking the binding sites of VEGF-A and VEGF-B inhibits VEGFR-1/-2 driven angiogenesis, tumor growth and metastasis. *Sci. Rep.* **8**(1), 17924 (2018).
48. Miner, M. W. et al. Comparison of:(2 S, 4 R)-4-[18F] fluoroglutamine,[11 C] methionine, and 2-Deoxy-2-[18F] Fluoro-D-Glucose and two small-animal PET/CT systems imaging rat gliomas. *Front. Oncol.* **11**, 730358 (2021).

Acknowledgements

We extend our heartfelt gratitude to the individuals and institutions that supported this research, particularly the University of Tehran and the University of Guilan. We would like to specifically acknowledge the Preclinical Lab at Tehran University of Medical Sciences for their invaluable in vivo imaging services, as well as the Animal Core Facility at the Institute of Biochemistry and Biophysics, University of Tehran, for their exceptional technical expertise. Additionally, we appreciate Dr. H. Rezaei Rudmianeh for her assistance.

Author contributions

Tahereh Rahdari: Writing – original draft and preparing the figures, Validation, Investigation, Methodology, Formal analysis, Data curation, Conceptualization. Mohsen Mahdavimehr: Investigation. Hossein Ghafouri: review & editing, Supervision, Resources, Validation, Project administration, Investigation, Conceptualization. Sorour Ramezanpour: Visualization, Validation, Resources, Methodology, Investigation. Somayeh Ehtesham: Investigation. S. Mohsen Asghari: Writing – review & editing, Supervision, Resources, Project administration, Data curation, Conceptualization.

Declarations

Competing interests

The authors declare no competing interests.

Ethics approval

All animal experiments were conducted following ethical guidelines and received approval from the Ethics Committee in Biomedical Research at the University of Guilan (Approval code: IR.GUILAN.REC.1401.010). All experiments were performed in accordance with relevant guidelines and regulations. This study is reported in accordance with ARRIVE guidelines.

Consent for publication

All authors read and approved the manuscript.

Additional information

Supplementary Information The online version contains supplementary material available at https://doi.org/10.1038/s41598-025-90107-y.

Correspondence and requests for materials should be addressed to H.G. or S.M.A.

Reprints and permissions information is available at www.nature.com/reprints.

Publisher's note Springer Nature remains neutral with regard to jurisdictional claims in published maps and institutional affiliations.

Open Access This article is licensed under a Creative Commons Attribution-NonCommercial-NoDerivatives 4.0 International License, which permits any non-commercial use, sharing, distribution and reproduction in any medium or format, as long as you give appropriate credit to the original author(s) and the source, provide a link to the Creative Commons licence, and indicate if you modified the licensed material. You do not have permission under this licence to share adapted material derived from this article or parts of it. The images or other third party material in this article are included in the article's Creative Commons licence, unless indicated otherwise in a credit line to the material. If material is not included in the article's Creative Commons licence and your intended use is not permitted by statutory regulation or exceeds the permitted use, you will need to obtain permission directly from the copyright holder. To view a copy of this licence, visit http://creativecommons.org/licenses/by-nc-nd/4.0/.

© The Author(s) 2025